JACS
JOURNAL OF THE AMERICAN CHEMICAL SOCIETY
Article
pubs.acs.org/JACS

# Synthesis and Thermal Properties of Solid-State Structural Isomers: Ordered Intergrowths of SnSe and $MoSe_2$

Noel S. Gunning,[†] Joseph Feser,[‡] Matt Beekman,[§] David G. Cahill,[‡] and David C. Johnson*[,†]

[†]Department of Chemistry and Materials Science Institute, University of Oregon, Eugene, Oregon 97403, United States
[‡]Department of Material Science and Engineering and F. Seitz Materials Research Laboratory, University of Illinois at Urbana−Champaign, Urbana, Illinois 61801, United States
[§]Department of Natural Sciences, Oregon Institute of Technology, Klamath Falls, Oregon 97601, United States

**ABSTRACT:** A family of structural isomers $[(SnSe)_{1.05}]_m(MoSe_2)_n$ were prepared using the modulated elemental reactant method by varying the layer sequence and layer thicknesses in the precursor. By varying the sequence of Sn−Se and Mo−Se layer pairs deposited and annealing the precursors to self-assemble the targeted compound, all six possible isomers $[(SnSe)_{1.05}]_4(MoSe_2)_4$, $[(SnSe)_{1.05}]_3(MoSe_2)_3[(SnSe)_{1.05}]_1(MoSe_2)_1$, $[(SnSe)_{1.05}]_3(MoSe_2)_2[(SnSe)_{1.05}]_1(MoSe_2)_2$, $[(SnSe)_{1.05}]_2(MoSe_2)_3[(SnSe)_{1.05}]_2(MoSe_2)_1$, $[(SnSe)_{1.05}]_2(MoSe_2)_1[(SnSe)_{1.05}]_1(MoSe_2)_2[(SnSe)_{1.05}]_1(MoSe_2)_1$, and $[(SnSe)_{1.05}]_2(MoSe_2)_2[(SnSe)_{1.05}]_1(MoSe_2)_1[(SnSe)_{1.05}]_1(MoSe_2)_1$ were prepared. The structures were characterized by X-ray diffraction and electron microscopy which showed that all of the compounds have very similar *c*-axis lattice parameters and in-plane constituent lattice parameters yet distinct isomeric structures. These studies confirm that the structure, order, and thickness of the constituent layers match that of the precursors. The cross-plane thermal conductivity is found to be very low (~0.08 $Wm^{-1}$ $K^{-1}$) and independent of the number of SnSe−$MoSe_2$ interfaces within uncertainty. The poor thermal transport in these layered isomers is attributed to a large cross-plane thermal resistance created by SnSe−$MoSe_2$ and $MoSe_2$−$MoSe_2$ turbostratically disordered van der Waals interfaces, the density of which has less variation among the different compounds than the SnSe−$MoSe_2$ interface density alone.

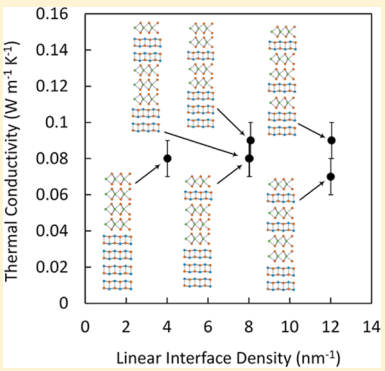


## 1. INTRODUCTION

The study and control of structure−function relationships in extended solids have frequently been frustrated by the difficulties in synthesizing materials with desired structures. The chemistry of solids with extended structures has largely been limited to thermodynamically stable phases as a result of the high temperatures used in synthesis to obtain reasonable diffusion rates and to promote atomic rearrangement.[1] While occasionally homologous series $A_nB_m$ with particular combinations *n* and *m* of structural fragments A and B can be purposely synthesized via traditional methods, this is not usually the case because such series are not often thermodynamically stable under the reaction conditions.[2−6] By contrast, the synthetic methods of organic molecular chemistry can readily prepare kinetically stable functional isomers, e.g., dimethyl ether and ethyl alcohol, which are compositionally identical but have vastly different properties. The level of synthetic control that is common in molecular chemistry has yet to be realized in the synthesis of inorganic extended solids because of the inability to control the kinetics of reactions with the necessary precision.[7,8] Although a systematic study of a series of specific compounds with distinct extended structures to probe the interplay of structure and properties can be imagined, in general the hypothetical compounds typically can not be prepared because of the lack of solid-state synthesis methods to form materials with specific targeted structures.

A number of nucleation-controlled approaches to extended solid-state compounds that involve preparing precursors, which do not require long-range diffusion, have been developed in attempts to gain kinetic control of the reaction pathways.[9−11] Low-temperature annealing of precursors prepared by codeposition onto a cold substrate has been successfully used to prepare new metastable compounds.[9] A similar approach, starting from sequentially deposited layers known as modulated elemental reactants, has also been used to prepare metastable compounds using composition as a way to control relative nucleation rates.[10,11] By preparing ordered sequences of bilayers of appropriate composition and thickness, this approach has been used to prepare families of compounds containing crystalline blocks of two different constituents with precise control of the relative thickness of each.[12−14] The self-assembly of the precursor does not require an epitaxial relationship between the constituent structures, relaxing constraints imposed by layer-by-layer growth. In fact, upon self-assembly, rotational disorder develops between the constituent blocks forming a disordered polymorph, and the

**Received:** April 27, 2015
**Published:** June 18, 2015



DOI: 10.1021/jacs.5b04351
J. Am. Chem. Soc. 2015, 137, 8803−8809

term ferecrystal has been coined to describe these compounds poised between the crystalline and amorphous states.[15−17] Very recently, this approach was used to prepare structural isomers, which feature identical numbers of layers of each constituent in the unit cell but varied sequences and thicknesses of individual blocks of these constituents, resulting in unique nanoarchitectures. Given just two constituents, A and B, with 1−10 layers of each constituent in the repeating unit, more than 20,000 specific A−B nanoarchitectures in principle can be formed.[18]

Reported here is the preparation of all of the possible structurally distinct isomers containing 4 SnSe rock salt bilayers and 4 $MoSe_2$ transition-metal dichalcogenide trilayers using the modulated elemental reactant synthesis approach. The ability to prepare these isomers permits, for the first time, the investigation of the effect of interface density on physical properties such as thermal conductivity without varying overall composition or the size of the unit cell. Thermal conductivity is an important property for a number of technological applications, and much attention has been paid to understanding how to both increase thermal conductivity for various heat transfer applications and decrease it for thermal barrier and thermoelectric applications. In prior studies on ferecrystals the ratio of the constituents has been shown to impact thermal conductivity.[17,19−21] Recent thermal conductivity measurements on $[(SnSe)_{1.05}]_m(MoSe_2)_n$ compounds having $m = n = 1−4$ showed that these compounds have cross-plane thermal conductivities independent of the repeat period (*c*-axis lattice parameter).[20] The suite of compounds in the SnSe−$MoSe_2$ system prepared in the present work allows a unique study of solid-state ferecrystal isomers that have the same composition but also the same *c*-axis lattice parameter and different number of SnSe/$MoSe_2$ interfaces in each "unit cell." There are two interfaces per unit cell in the **44** compound, four in the **3311**, **3212**, and **2321** compounds, and six in the **211211** and **221111** compounds as shown in Figure 1 (see Figure 1 for a graphical explanation of the shorthand notation ***mn***, where *m* is the number of axially oriented SnSe bilayers and ***n*** is the number of dichalcogenide trilayers, Se−Mo−Se). Previous studies of thermal conductivity in epitaxial superlattices, where the superlattice period defined the interface density, found systematic changes in thermal conductivity with superlattice period.[22−26] Based on previous studies of ferecrystals, which do not contain epitaxial interfaces, the thermal conductivity would be expected to be independent of SnSe−$MoSe_2$ interface density. The ability to prepare the structural isomers presented here has allowed us to confirm this hypothesis in a rare example of physical properties investigation of solid-state structural isomers.

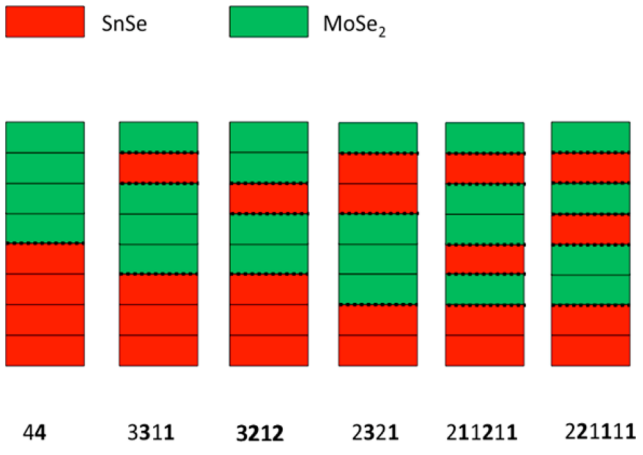


**Figure 1.** Schematic structures of the six possible isomers containing 4 SnSe bilayers and 4 $MoSe_2$ trilayers subunits and having the same axial period as the **44** compound are shown. Red and green blocks indicate the relative thickness and sequence of the different constituent compounds, respectively. The compound $[(SnSe)_{1.05}]_4(MoSe_2)_4$, which contains a block of four rock salt structured bilayers and a block of four dichalcogenide trilayers, is abbreviated as **44**. **211211** is the abbreviation for the compound $[(SnSe)_{1.05}]_2(MoSe_2)_1[(SnSe)_{1.05}]_1(MoSe_2)_2[(SnSe)_{1.05}]_1(MoSe_2)_1$.

## 2. EXPERIMENTAL SECTION

Ferecrystal thin films were prepared on ⟨100⟩ Si substrates in a deposition chamber evacuated to $10^{-8}$ Torr using the modulated elemental reactants technique described previously.[27,28] Tin granules of 99.5%+ purity from Aldrich Chemicals, molybdenum rods of 99.95% purity from Alfa Aesar, and amorphous selenium shot of 99.999% purity from Alfa Aesar were used as purchased. Sn and Mo were evaporated using Thermionic electron-beam guns, and Se was evaporated using a resistively heated Knudsen cell. Deposition rates and thicknesses were controlled by quartz crystal microbalances with appropriate tooling factors to account for the geometry of the chamber.[29] The shutters positioned over each source were used to control the deposition using an integrated computer program.

After deposition, samples were annealed on a hot plate (hot plate temperature of 450 °C) for 30 min in a $N_2$ drybox with <1 ppm oxygen. X-ray reflectivity (XRR) and X-ray diffraction (XRD) were performed using a Bruker D8 Discover with Cu K$\alpha$ radiation. In-plane synchrotron X-ray diffraction data were collected at the Advanced Photon Source, Argonne National Lab, Beamline-33-C or on a Rigaku SmartLab equipped with Cu K$\alpha$ (0.154 nm) radiation. Electron probe microanalysis (EPMA) was used to determine the composition. Data were collected at different accelerating voltages on a Cameca SX-50 and analyzed using a previously reported technique.[30,31]

Scanning transmission electron microscopy (STEM) data was collected on a spherical aberration (image) corrected FEI Titan operated at 300 kV and equipped with a high angle annular dark field (HAADF) detector.

Thermal conductivity experiments were performed at room temperature using time-domain thermoreflectance as described previously.[32,33]

## 3. RESULTS AND DISCUSSION

The synthesis of the title compounds was carried out in a manner described in detail previously.[34] In order to synthesize structural isomers, we first calibrated the deposition parameters for a binary Mo−Se film containing alternating layers of Mo and Se and a similar Sn−Se film to obtain compositions corresponding to the targeted SnSe and $MoSe_2$ constituent stoichiometries, with ∼5 atomic % excess of Se to compensate for losses that occur during annealing. Films containing the four layer sequence Mo−Se−Sn−Se were then deposited holding the Mo−Se and Sn−Se atomic ratios constant but adjusting the relative thickness of each elemental bilayer to obtain an Sn:Mo ratio $(1 + \delta)$ of 1.05; $1 + \delta$ represents the difference in the cation density per unit area of the adjacent planes of the crystalline SnSe and $MoSe_2$ constituents. The absolute thickness was then scaled holding all of the atomic ratios constant to provide the number of atoms required to form a bilayer of SnSe and a crystallographic unit (a Se−Mo−Se trilayer) of $MoSe_2$. Using these calibrated thicknesses, two sets of six precursors were prepared corresponding to the six layer sequences of the structural isomers shown in Figure 1. These


DOI: 10.1021/jacs.5b04351
J. Am. Chem. Soc. 2015, 137, 8803−8809

designed precursors were then annealed as described previously to self-assembly into the desired products.[34]

XRD and XRR scans, shown in Figures 2 and 3, were collected to study the structure of the self-assembled isomers.

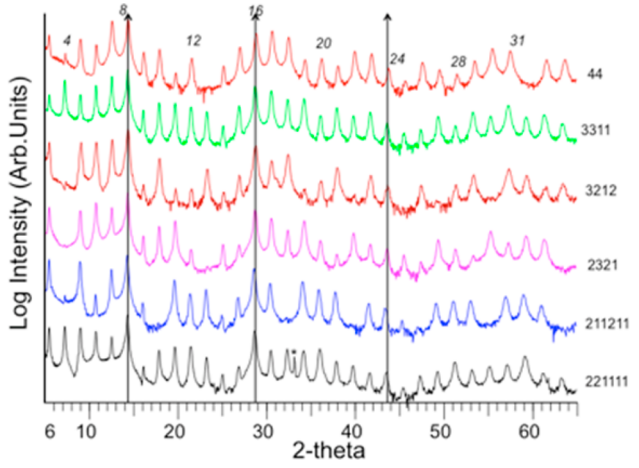


**Figure 2.** Specular XRD patterns of the six isomers, vertically displaced for clarity. The numbers above selected peaks of the top pattern indicate (00*l*) Miller indices of selected reflections of the isomers. The vertical lines are drawn to highlight that each of the isomers have nearly the same *c*-axis lattice parameter. The peak marked by an asterisk in the scan of the **221111** isomer is a Si substrate reflection.

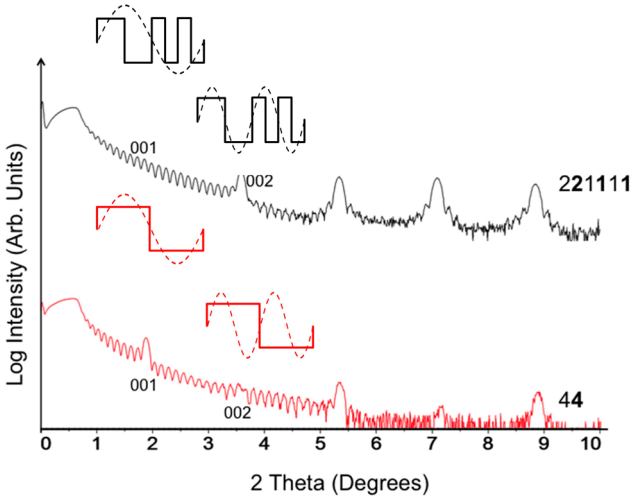


**Figure 3.** X-ray reflectivity scans for the **44** and **221111** isomers. The scans have been vertically displaced for clarity. The inset figures above the **221111** and **44** data sets contain approximations of the electron density change along the *c* axis of the isomers, with the constituents having different but constant electron density profiles and an abrupt interface between them. The superimposed dashed curves are the respective Fourier components for the (001) and (002) reflections. (Note that the electron density and Fourier component are schematically plotted on top of each other but do not have the same zero reference, i.e., the electron density is strictly positive, whereas the Fourier component oscillates between positive and negative values.)

All of the Bragg maxima could be indexed as (00*l*) reflections of the superlattice indicating preferred crystallographic alignment. The presence of well-defined, high-order reflections in the XRD data indicates a high degree of structural order and coherent diffraction from the intergrowth structure along the *c*-axis. The *c*-axis lattice parameters were calculated from the positions of these reflections using Bragg's law and are summarized in Table 1. Despite the different number of SnSe–$MoSe_2$ interfaces per unit cell in the isomers (two in **44**, four in **3212**, **2321**, and **3311**, and six in **211211** and **221111**), the *c*-axis lattice parameters of all the isomers in each sample set are similar and reproducible. The small changes in the *c*-axis lattice parameter within each set and the slightly larger *c*-axis lattice parameters measured for the second set reflect the precision of the deposition control required to reproduce the samples. The well-defined Kiessig fringes in the XRR data (Figure 3) indicate that the front and back of the film are smooth and parallel to one another, a consequence of the ordered stacking of the constituent layers. Using the relationship derived by Parratt and estimating that Kiessig fringes are no longer visible at approximately 12° 2$\theta$, we estimate the average roughness of the films to be near 1.2 Å.[35,36]

While the variation in the position of the reflections and therefore unit cell sizes is small, there are pronounced changes in the relative intensities of reflections in the diffraction patterns. Since the diffracted intensity in these specular XRD patterns is proportional to the Fourier transform of the electron density profile along the axial direction, the variation in relative intensities reflects the different stacking sequence of the constituents in the isomeric intergrowths. For example, the XRR pattern of the 221111 isomer, shown in Figure 3, has a weak (001) and a strong (002) reflection, while the relative intensities of these reflections are reversed in the **44** isomer. The intensity of the $(00l)^{th}$ reflection in each case is proportional to the integral of the product of the electron density profile and the respective Fourier component.

To illustrate the origin of the different relative intensities qualitatively, the inset in Figure 3 shows a simplified step function approximation of the average electron density profile for both the **44** and **221111** isomers, with each of the constituent compounds approximated as having a different magnitude but constant electron density. The step widths mimic the different layer arrangements in the unit cells, and the interfaces are assumed to be abrupt changes in electron density. The sine function describing the Fourier component of the (001) and (002) reflections is superimposed on the electron density for both isomers. The integral of the product of the sine function and the electron density for the (001) reflection results in a positive number for the first half of the unit cell and a smaller negative number for the second half of the unit cell, resulting in a significant (00l) reflection intensity. By contrast, for the (002) reflection the positive integral for the first quarter of the unit cell is exactly canceled by the second quarter, and the integral in the third and fourth quarters of the unit cell also exactly cancel, so the integral of the product of the sine function and the electron density is zero and no intensity is observed. For the 221111 isomer, the integral of the product of the sine function and the electron density for the (001) reflection is near zero because the positive integral in the first half of the unit cell is nearly exactly canceled by the negative integral from the second half of the unit cell. For the (002) reflection, we get a positive number for the integral over the first half of the unit cell and zero for the integral over the second half, leading to measurable intensity for the 002 reflection.

Further evidence that the intended structures of the isomers have been formed is provided by HAADF-STEM images, which are shown in Figure 4. The STEM images all indicate two different structural units, highlighted by red and green shading


DOI: 10.1021/jacs.5b04351
J. Am. Chem. Soc. 2015, 137, 8803–8809

**Table 1. Total Thickness and *a*- and *c*-Axes Lattice Parameters for the Two Sample Sets of Isomers Calculated from the XRR and XRD Data, Respectively**

| | sample set 1 | | | | sample set 2 | |
|---|---|---|---|---|---|---|
| sample | total thickness (nm) | *c*-axis lattice parameter (nm) | *a*-axis lattice parameter SnSe (nm) | *a*-axis lattice parameter $MoSe_2$ (nm) | total thickness (nm) | *c*-axis lattice parameter (nm) |
| **44** | 64.7(1) | 4.972(7) | 0.604(2) | 0.331(1) | 64.8(1) | 4.98(1) |
| **3311** | 64.7(1) | 4.977(5) | 0.604(1) | 0.331(1) | 64.9(1) | 4.997(5) |
| **3212** | 64.3(1) | 4.947(7) | 0.603(1) | 0.331(1) | 64.8(1) | 4.99(1) |
| **2321** | 64.9(1) | 4.993(8) | 0.602(2) | 0.331(1) | 64.9(1) | 4.997(1) |
| **211211** | 65.0(1) | 4.997(5) | 0.603(1) | 0.333(1) | 64.9(1) | 4.99(1) |
| **221111** | 64.8(1) | 4.98(1) | 0.602(1) | 0.332(1) | 65.1(1) | 5.009(3) |

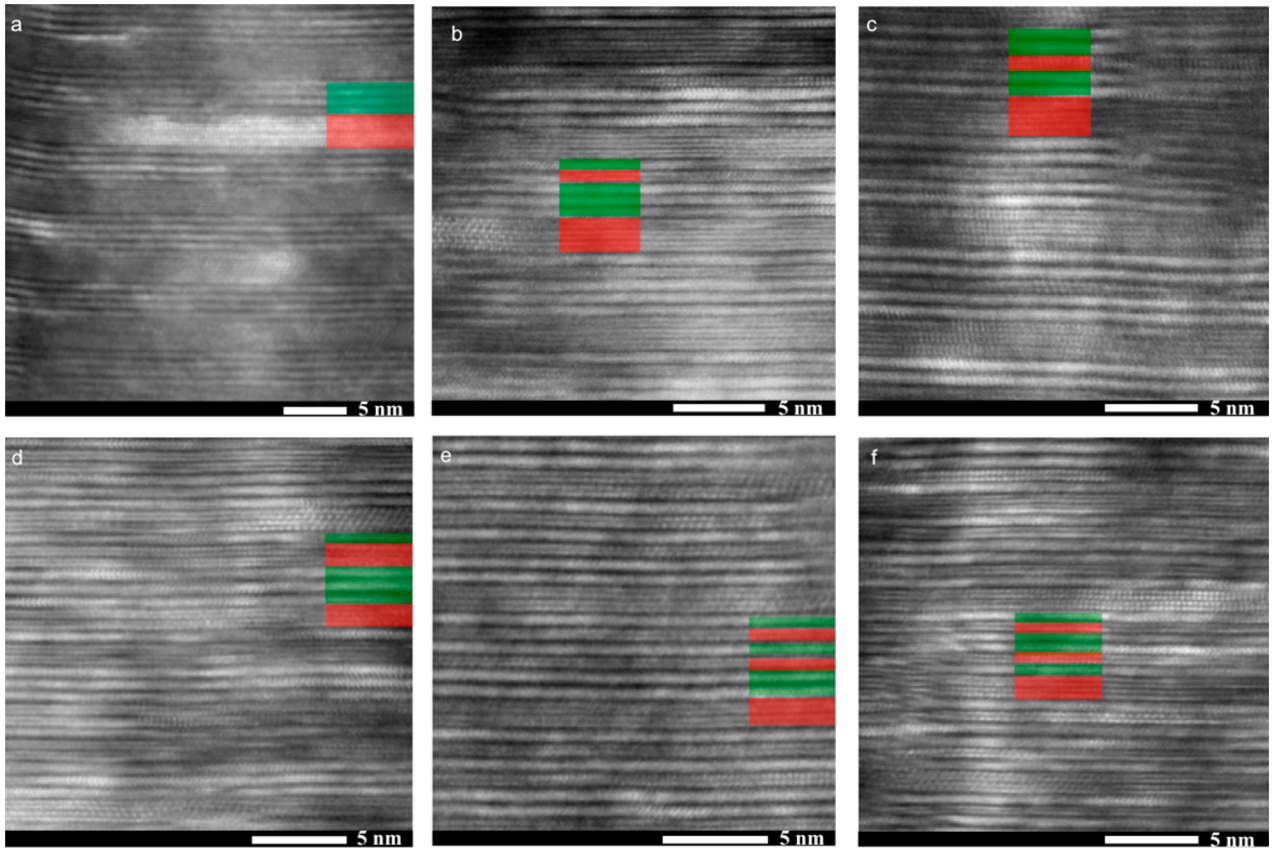


**Figure 4.** Cross-sectional HAADF-STEM images of the six structural isomers: (a) **44**, (b) **3311**, (c) **3212**, (d) **2321**, (e) **221111**, and (f) **211211** isomers.

in part of each figure. Each image shows the different stacking sequences of these structural units that are expected for each of the distinct structural isomers. The red layers in the insets of the figures highlight the SnSe subunits, which consist of bilayers that have a distorted rock salt structure.[34] In different regions of the isomers, both (100) and (110) crystal orientations can be identified. These orientations occur with no regular periodicity and also can both occur in the same layer as a result of finite in-plane domain size. There are also no long-range correlations between crystal orientations, which is typical of turbostratically disordered constituents.[16,17,20,37] The green insets of the figures highlight the $MoSe_2$ subunits, which have a trilayer topology where a hexagonal sheet of Mo atoms is sandwiched between two hexagonal sheets of Se. The distinct layers can be observed in regions in the images of Figure 4 where the view is along a zone axis. Both (110) and (120) orientations can be found, and the chevron (120) orientation indicates that the Mo atoms have trigonal prismatic coordination. Adjacent dichalcogenide subunits also commonly do not possess the same crystal orientation, reflecting the turbostratic disorder of interleaved structures formed using this synthetic approach.[38]

In order to obtain additional in-plane structural information, grazing incidence (in-plane) XRD was performed and is shown in Figure 5. The in-plane scans contain Bragg reflections originating from the individual SnSe and $MoSe_2$ building blocks that can be indexed as (*hk*0) reflections from their respective NaCl-like and $CdI_2$ structure types. In contrast to the marked intensity variations observed in Figure 2, the relative intensities of the broad reflections in the in-plane diffraction data do not vary much between the different isomers, even for reflections at high angles, because each of the isomers has the same number of layers of each constituent, which diffract independent due to the turbostratic disorder. The indexed reflections shown in Figure 5 were used to calculate the in-plane unit cell parameters of each subunit for all the isomers, which are summarized in Table 1. They are similar to previously reported values, which


DOI: 10.1021/jacs.5b04351
*J. Am. Chem. Soc.* 2015, 137, 8803−8809

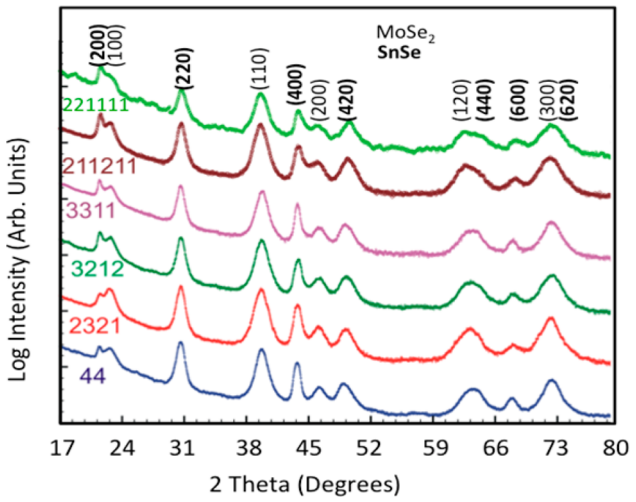


**Figure 5.** In-plane XRD scans of the six isomers. The (*hk*0) indices for the two constituents are given above the diffraction pattern of the **221111** isomer.

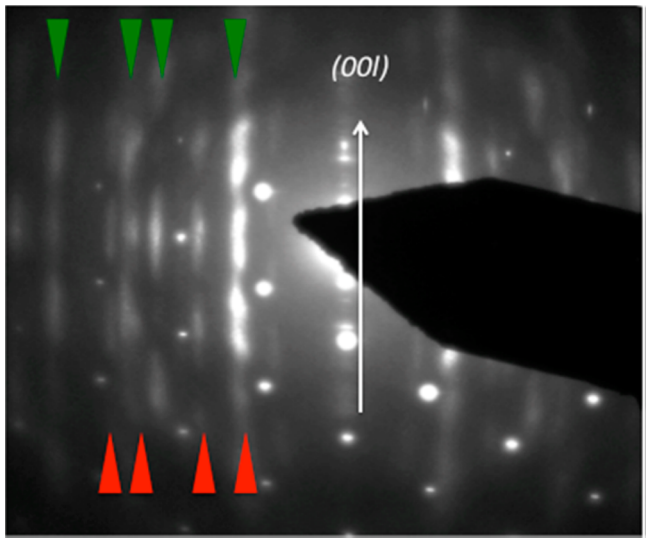


**Figure 6.** Selected area electron diffraction pattern of the **3212** isomer. Some of the identifiable families of *hkl* reflections of the individual constituents SnSe (red) and $MoSe_2$ (green) are indicated. The hexagonal pattern of sharp spots is caused by the silicon substrate.

range between 0.6003(1) and 0.601 nm for the *a* axis lattice parameter of SnSe and between 0.331(1) and 0.3320(1) nm for the *a* axis lattice parameter of $MoSe_2$.[37,39] The calculated in-plane lattice parameter for SnSe is consistent with other reported $[(SnSe)_{1+y}]_m(TSe_2)_n$ compounds, where (T = Ti, V, Ta, Nb), which range between 0.5935(4) and 0.605(9) nm.[13,36,38,40] The in-plane lattice parameter of the SnSe constituent is also similar to that reported for misfit layered compounds containing SnSe.[41] The in-plane $MoSe_2$ lattice parameters are similar to $(PbSe)_{0.99}MoSe_2$, *a* = 0.3308(4) nm,[12] and marginally larger than the $MoSe_2$ itself, 0.329(1) nm.[42] Our observed value for the misfit parameter, 1.05, is within the error of that reported previously, 1.04,[20,34,39] indicating that the constituents in these structural isomers are structurally similar to the constituents in other known compounds in this system.

The preferred crystallographic alignment of the films results in only (00*l*) and (*hk*0) reflections observed in the specular and in-plane diffraction patterns, respectively. To obtain information on the stacking of the constituent layers, selected area electron diffraction patterns were obtained on cross-sectioned samples with the electron beam directed perpendicular to the *c*-axis of the intergrowth. Figure 6 contains a representative electron diffraction pattern for the **3212** isomer. For reference, the (00*l*) reflections at the center of the diffraction pattern correlate with the specular pattern in Figure 2. Additional (*hkl*) reflections can be attributed to the individual SnSe and $MoSe_2$ components. The elongation or smearing of these reflections along the *c**-axis corroborates the turbostratic disorder observed in the HAADF-STEM images. The broadening of the reflections is caused by the lack of interlayer long-range order, essentially making each constituent layer an independently diffracting domain.

The thermal conductivity data for the isomers are listed in Table 2. The values of the isomers are all the same within error and extremely small for dense solids, ~0.08 $Wm^{-1}K^{-1}$, and the value obtained for the **44** compound is in good agreement with the value measured for a different sample in our previous work.[20] These thermal conductivities are smaller than those reported for amorphous solids such as inorganic glasses or organic polymers, which typically have thermal conductivities near 1 and 0.2 $Wm^{-1}K^{-1}$, respectively. Similar extremely small

**Table 2. Total Cross-Plane Thermal Conductivity of the Six Isomers and Electrical Component of the In-Plane Thermal Conductivity Calculated from In-Plane Electrical Resistivity Using the Wiedemann–Franz Law**[a]

| | sample set 1 | sample set 2 | |
|---|---|---|---|
| sample | total cross-plane thermal conductivity ($Wm^{-1}K^{-1}$) | in-plane electrical resistivity (mΩ·m) | electrical component in-plane thermal conductivity ($Wm^{-1}K^{-1}$) |
| **44** | 0.08(1) | 12.8 | 0.0006 |
| **3311** | 0.08(1) | 4.05 | 0.002 |
| **3212** | 0.09(1) | 7.22 | 0.001 |
| **2321** | 0.08(1) | 1.45 | 0.005 |
| **211211** | 0.07(1) | 1.37 | 0.005 |
| **221111** | 0.09(1) | 1.76 | 0.004 |

[a]All data were collected at room temperature.

values for the thermal conductivity were reported previously for both $[(PbSe)_{0.99}]_m(MoSe_2)_n$ and $[(PbSe)_{1.00}]_m(WSe_2)_n$.[12,21] The values measured for ferecrystal compounds are more comparable to values reported for porous solids such as aerogels,[43] in spite of the fact that the ferecrystals are dense solids. In these families of compounds, the thermal conductivity depended on the relative composition, (the *m*/n ratio), but were relatively independent of the size of the *c*-axis lattice parameter.[12,19,20] The extremely small thermal conductivity of $WSe_2$ was a consequence of the turbostratic disorder,[43] suggesting that the turbostratic disorder observed for the isomers is the underlying cause of the unusually small thermal conductivity.

In order to estimate the electronic contribution to the thermal conductivity, in-plane electrical resistivity was measured. These values are contained in Table 2 and are between 1–10 mΩ·m. Assuming isotropic in-plane electrical conductivity in these compounds and using the Wiedemann–Franz expression with the free-electron Lorenz constant $2.45 \times 10^{-8}$ $W\Omega K^{-2}$, we estimate the in-plane electrical contribution of thermal conductivity as summarized in Table 2. The electrical contribution to the in-plane thermal conductivity, using this


DOI: 10.1021/jacs.5b04351
J. Am. Chem. Soc. 2015, 137, 8803–8809

approximation, ranges from ~$10^{-4}$ to $10^{-3}$ $Wm^{-1}$ $K^{-1}$. Prior reports on the anisotropy of electrical conductivity in the structurally related misfit layered compounds found that the cross-plane electrical conductivity can be 30−250 times smaller than in-plane electrical conductivity.[44−46] We therefore conclude that the electronic contribution to the cross-plane thermal conductivity is significantly <~$10^{-4}$−$10^{-3}$ $Wm^{-1}$ $K^{-1}$ and the measured cross plane thermal conductivity is dominated by the lattice contribution.

The density of SnSe−$MoSe_2$ interfaces appears to have no influence on the cross-plane thermal conductivity of these isomers. When the bulk phonon mean free path is smaller than the superlattice period for an epitaxial superlattice composed of constituents A and B, the total thermal resistance is approximately the sum of the thermal resistance of the A−B interfaces, $R_i$ and the resistances of layers $R_A$ and $R_B$, so $R_T = \sum R_A + \sum R_B + \sum R_i$.[47,48] However, the ferecrystal intergrowths described here are not epitaxial and have relatively short periods. We attribute the constant thermal conductivity, independent of the density of SnSe−$MoSe_2$ interfaces, to the turbostratic disorder discussed above. The number of SnSe−$MoSe_2$ interfaces varies from two (for the **44**) to six (for the **211211** and **221111**) per repeat period (a 200% increase in interface density). In contrast, noting that there is $MoSe_2$−$MoSe_2$ and $MoSe_2$−SnSe but not SnSe−SnSe turbostratic disorder,[39] the total number of turbostratically disordered interfaces only varies from five to seven per repeat period (a 40% increase in interface density, assuming that each $MoSe_2$ is turbostratically disordered with respect to an adjacent $MoSe_2$ layer). In spite of the much lower cross-plane thermal conductivity of layered SnSe (~0.5 $Wm^{-1}$ $K^{-1}$)[49] relative to that of cubic PbSe (>2.5 $Wm^{-1}$ $K^{-1}$),[50] SnSe−$MoSe_2$ ferecrystals have thermal conductivities comparable to PbSe−$MoSe_2$ intergrowths,[12] further evidence that supports the conclusion that turbostratic disorder is the thermal transport-limiting feature in these materials.

Turbostratic disorder has been shown[43] to produce a thermal conductivity lower than the theoretical minimum predicted by Cahill, Watson, and Pohl.[51] The Cahill−Watson−Pohl model assumes an isotropic solid and is based on the idea that the minimum thermal conductivity results when the heat transport can be described by a random walk of thermal energy from atom to atom (or groups of atoms) with a jump time equal to one-half of the period of atomic vibration. For an amorphous solid, the rate of transfer of energy would therefore be the same in every direction. In the materials studied here, the rotational disorder of the *a*−*b* planes between the constituents and within the $MoSe_2$ layers makes the sample effectively amorphous in the c direction. There is longer-range crystallographic order and strong bonding, however, in the *a*−*b* plane of the SnSe blocks and in each single layer of $MoSe_2$. The presence of in-plane phonons combined with the structural incoherence between the $MoSe_2$ layers enables efficient in-plane energy transfer and a reduced rate of energy transfer in the *c*-axis direction, respectively.[52]

The ability to intentionally synthesize isomers with different interface densities but identical composition and *c*-axis lattice parameters enables us to eliminate differences in unit cell size as a factor when probing the effect of interface density on thermal conductivity. The independence of the thermal conductivity from the number of SnSe−$MoSe_2$ interfaces per unit cell in the set of isomers and on the size of the blocks of each constituent supports the hypothesis that the low lattice thermal conductivity of these and related dichalcogenide containing ferecrystals results from $MoSe_2$−$MoSe_2$ and $MoSe_2$−SnSe turbostratic disorder in these ferecrystal intergrowths.

## 4. CONCLUSIONS

The use of designed precursors enabled us to self-assemble all six possible solid-state structural isomers comprised of four Sn−Se rock salt structured bilayers and four Se−Mo−Se trigonal prismatic transition-metal dichalcogenide structured trilayers. This ability to make a large number of structurally related materials having the same composition but different structure enables a new level of investigation where specific material parameters can be held constant, while others are varied to individually probe specific structure−property relationships. In this study we held composition and *c*-axis lattice parameter constant, while varying SnSe−$MoSe_2$ interface density, and discovered that the thermal conductivity of these ferecrystal isomers does not depend on the SnSe−$MoSe_2$ interface density. The ability to intentionally synthesize a structurally related series of compounds in solid-state chemistry is analogous to the approaches used extensively in molecular chemistry to correlate functional groups with properties. Achieving a comparable level of synthetic control in extended inorganic chemistry would provide transformative opportunities to explore and utilize structure−function relationships in functional materials.

## AUTHOR INFORMATION

### Corresponding Author

*davej@uoregon.edu

### Notes

The authors declare no competing financial interest.

## ACKNOWLEDGMENTS

The authors acknowledge support from the National Science Foundation under grant DMR-1266217 and CHE-1102637. Grant MRI 0923577 provided funding for the dual beam FIB used to make TEM cross sections.

## REFERENCES

(1) Corbett, J. D. Synthesis of Solid-State Materials. In *Solid State Chemistry, Techniques*; Cheetham, A. K., Day, P., Eds.; Clarendon Press: Oxford, 1987; Vol. *1*, pp 1−38.
(2) Fluck, E.; Binder, H. *Z. Anorg. Allg. Chem.* **1967**, *354*, 113−129.
(3) Ohta, H.; Seo, W.-S.; Koumoto, K. *J. Am. Ceram. Soc.* **1996**, *79*, 2193−2196.
(4) Michiue, Y.; Kimizuka, N. *AActa Crystallogr., Sect. B* **2010**, *66*, 117.
(5) Mori, T.; Nishimura, T. *J. Solid State Chem.* **2006**, *179*, 2908−2915.
(6) Mori, T.; Nishimura, T.; Schnelle, W.; Burkhardt, U.; Grin, Y. *Dalton Trans.* **2014**, *43*, 15048−15054.
(7) Disalvo, F. J. *Science* **1990**, *247*, 649−55.
(8) Stein, A.; Keller, S. W.; Mallouk, T. E. *Science* **1993**, *259*, 1558.
(9) Liebold-Ribeiro, Y.; Fischer, D.; Jansen, M. *Angew. Chem., Int. Ed.* **2008**, *47*, 4428−4431.
(10) Behrens, M.; Kiebach, R.; Bensch, W.; Häussler, D.; Jäger, W. *Inorg. Chem.* **2006**, *45*, 2704−2712.
(11) Smalley, A. L. E.; Jespersen, M. J.; Johnson, D. C. *Inorg. Chem.* **2004**, *43*, 2486−2490.
(12) Heideman, C. L.; Tepfer, S.; Lin, Q.; Rostek, R.; Zschack, P.; Anderson, M. D.; Anderson, I. M.; Johnson, D. C. *J. Am. Chem. Soc.* **2013**, *135*, 11055−11062.


DOI: 10.1021/jacs.5b04351
*J. Am. Chem. Soc.* 2015, 137, 8803−8809

(13) Atkins, R.; Disch, S.; Jones, Z.; Haeusler, I.; Grosse, C.; Fischer, S. F.; Neumann, W.; Zschack, P.; Johnson, D. C. *J. Solid State Chem.* **2013**, *202*, 128−133.
(14) Beekman, M.; Cogburn, G.; Heideman, C.; Rouvimov, S.; Zschack, P.; Neumann, W.; Johnson, D. C. *J. Electron. Mater.* **2012**, *41*, 1476−1480.
(15) Beekman, M.; Heideman, C. L.; Johnson, D. C. *Semicond. Sci. Technol.* **2014**, *29*, 064012/1−064012/14.
(16) Moore, D. B.; Beekman, M.; Disch, S.; Zschack, P.; Hausler, I.; Neumann, W.; Johnson, D. C. *Chem. Mater.* **2013**, *25*, 2404−2409.
(17) Mortensen, C.; Beekman, M.; Johnson, D. C. *Sci. Adv. Mater.* **2011**, *3*, 639−645.
(18) Esters, M.; Alemayehu, M. B.; Jones, Z.; Nguyen, N. T.; Anderson, M. D.; Grosse, C.; Fischer, S. F.; Johnson, D. C. *Angew. Chem., Int. Ed. Engl.* **2015**, *54*, 1130−1134.
(19) Chiritescu, C.; Cahill, D. G.; Heideman, C.; Lin, Q.; Mortensen, C.; Nguyen, N. T.; Johnson, D.; Rostek, R.; Böttner, H. *J. Appl. Phys.* **2008**, *104*, 33533−33538.
(20) Gunning, N. S.; Feser, J.; Falmbigl, M.; Beekman, M.; Cahill, S. G.; Johnson, D. C. *Semicond. Sci. Technol.* **2014**, *29*, 1−8.
(21) Lin, Q.; Smeller, M.; Heideman, C. L.; Zschack, P.; Koyano, M.; Anderson, M. D.; Kykyneshi, R.; Keszler, D. A.; Anderson, I. A.; Johnson, D. C. *Chem. Mater.* **2010**, *22*, 1002−1009.
(22) Chen, G. *J. Heat Trans.* **1997**, *119*, 220−229.
(23) Huxtable, S. T.; Abramson, A. R.; Tien, C.; Majumdara, A.; Shakouri, A.; Croke, E. T. *Appl. Phys. Lett.* **2002**, *80*, 1737−1739.
(24) Lee, S. M.; Cahill, D. G.; Venkatasubramanian, R. *Appl. Phys. Lett.* **1997**, *70*, 2957−2959.
(25) Capinski, W. S.; Maris, H. J. *Physica B* **1996**, *219*, 699−701.
(26) Chen, G.; Tien, C. L.; Wu, X.; Smith, J. S. *J. Heat Trans.* **1994**, *116*, 325−331.
(27) Harris, F. R.; Standridge, S.; Johnson, D. C. *J. Am. Chem. Soc.* **2005**, *127*, 7843−7848.
(28) Nguyen, N. T.; Howe, B.; Hash, J. R.; Liebrecht, N.; Johnson, D. C. *Adv. Mater.* **2006**, *18*, 118−122.
(29) Fister, L.; Le, X. M.; McConnell, J.; Novet, T.; Johnson, D. C. *J. Vac. Sci. Technol. A* **1993**, *11*, 3014−3019.
(30) Donovan, J. J.; Tingle, T. N. *J. Microsc. Soc. Am.* **1996**, *2*, 1−7.
(31) Donovan, J. J.; Snyder, D. A.; Rivers, M. L. *Microbeam Anal.* **1993**, *2*, 23−8.
(32) Cahill, D. G. *Rev. Sci. Instrum.* **2004**, *75*, 5119−5122.
(33) Costescu, R. M.; Wall, M. A.; Cahill, D. G. *Phys. Rev. B* **2003**, *67*, 054302/1−054302/5.
(34) Beekman, M.; Disch, S.; Gunning, N.; Johnson, D. C. *Inorg. Chem.* **2015**, *54*, 1091−1099.
(35) Partatt, L. G. *Phys. Rev.* **1954**, *95*, 359−69.
(36) Merrill, D. R.; Moore, D. B.; Ditto, J.; Sutherland, D. R.; Falmbigl, M.; Winkler, M.; Pernau, H.-F.; Johnson, D. C. *Eur. J. Inorg. Chem.* **2015**, 83−91.
(37) Smeller, M. M.; Heideman, C. L.; Lin, Q.; Beekman, M.; Anderson, M. D.; Zschack, P.; Anderson, I. M.; Johnson, D. C. *Z. Anorg. Allg. Chem.* **2012**, *638*, 2632−2639.
(38) Atkins, R.; Wilson, J.; Zschack, P.; Grosse, C.; Neumann, W.; Johnson, D. C. *Chem. Mater.* **2012**, *24*, 4594−4599.
(39) Beekman, M.; Disch, S.; Rouvimov, S.; Kasinathan, D.; Koepernik, K.; Rosner, H.; Zschack, P.; Neumann, W. S.; Johnson, D. C. *Angew. Chem., Int. Ed.* **2013**, *52*, 13211−13214.
(40) Alemayehu, M. B.; Falmbigl, M.; Grosse, C.; Ta, K.; Fischer, S. F.; Johnson, D. C. *J. Alloys Compd.* **2015**, *619*, 861−868.
(41) Wiegers, G. A.; Zhou, W. Y. *Mater. Res. Bull.* **1991**, *26*, 879−885.
(42) Bronsema, K. D.; De Boer, J. L.; Jellinek, F. *Z. Anorg. Allg. Chem.* **1986**, *540*, 15−17.
(43) Chiritescu, C.; Cahill, D. G.; Nguyen, N.; Johnson, D.; Bodapati, A.; Keblinski, P.; Zschack, P. *Science* **2007**, *315*, 351−3.
(44) Wiegers, G. A.; Meetsma, A.; Haange, R. J.; De Boer, J. L. *J. Sol. St. Chem.* **1990**, *89*, 328−339.
(45) Nadar, A. *Phys. Status Solidi C* **2006**, *3*, 2972−2974.
(46) Wiegers, G. A. *Prog. Solid State Chem.* **1996**, *24*, 1−139.
(47) Cahill, D. G.; Braun, P. V.; Chen, G.; Clarke, D. R.; Fan, S.; Goodson, K. E.; Keblinski, P.; King, W. P.; Mahan, G. D.; Majumdar, A.; Maris, H. J.; Phillpot, S. R.; Pop, E.; Shi, L. *Appl. Phys. Rev.* **2014**, *1*, 011305/1−011305/45.
(48) Cahill, D. G.; Ford, W. K.; Goodson, K. E.; Mahan, G. D.; Majumdar, A.; Maris, H. J.; Merlin, R.; Phillpot, S. R. *J. Appl. Phys.* **2003**, *93*, 793.
(49) Zhao, L. D.; Lo, S. H.; Zhang, Y.; Sun, H.; Tan, G.; Uher, C.; Wolverton, C.; Dravid, V. P.; Kanatzidis, M. G. *Nature* **2014**, *508*, 373−377.
(50) Pei, Y.; Shi, X.; LaLonde, A.; Wang, H.; Chen, L.; Snyder, G. J. *Nature* **2011**, *473*, 66−69.
(51) Cahill, D. G.; Watson, S. K.; Pohl, R. O. *Phys. Rev. B* **1992**, *46*, 6131−6140.
(52) Hopkins, P. E.; Piekos, E. S. *Appl. Phys. Lett.* **2009**, *94*, 181901.


DOI: 10.1021/jacs.5b04351
*J. Am. Chem. Soc.* 2015, 137, 8803−8809